GSA Data Repository 2015086
Grainsize Distributions from Figure1 xlsx file

Supplementary Information

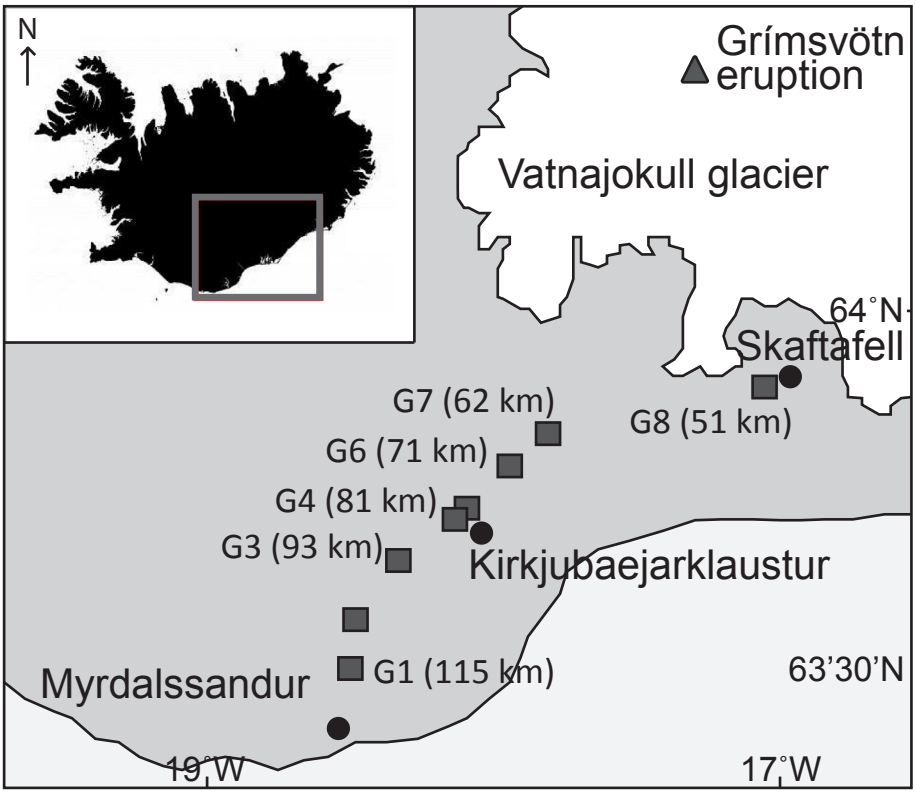

Supplementary information, Figure S1. Location map showing the 2011 vent (triangle) and sampling sites along the dispersal axis (squares). Coordinates given in Olsson et al., (2013). Samples used in this study are labelled with their distance from the vent.

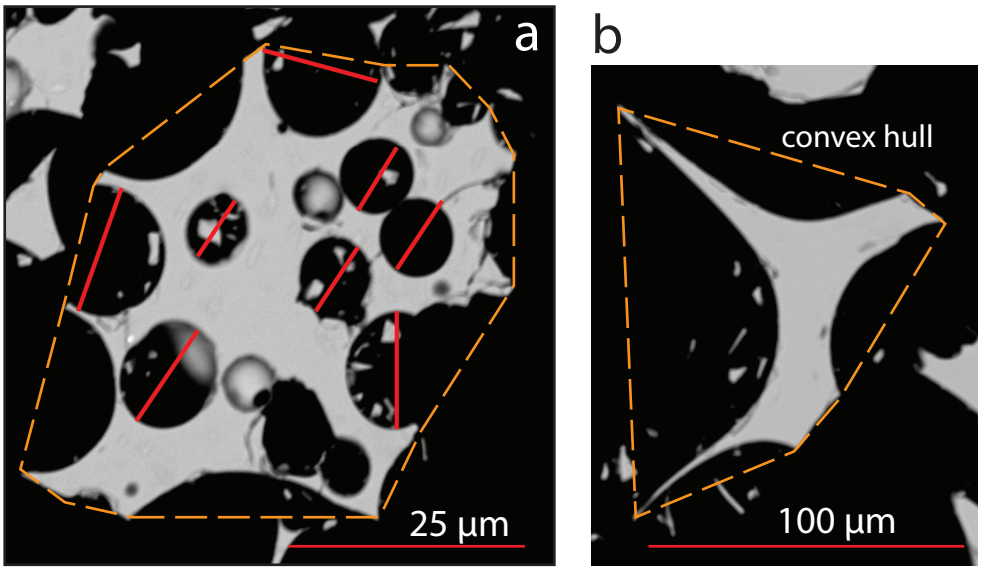

Supplementary information, Figure S2. A: measurement of vesicle diameters. We determined the maximum dimension (red lines) of 250 bubbles per size fraction from BSE grid images, including all vesicles >2 µm that preserved at least 50% of the bubble wall. B: The smooth concave curvature on even the largest shards provides evidence of some larger vesicles that are not captured by our measured VSD. The dashed orange lines illustrate the convex hull for the two particles shown in A and B. The convex hull perimeter is like stretching an elastic band around a particle, and is equivalent to the particle outline for a fully convex shape.

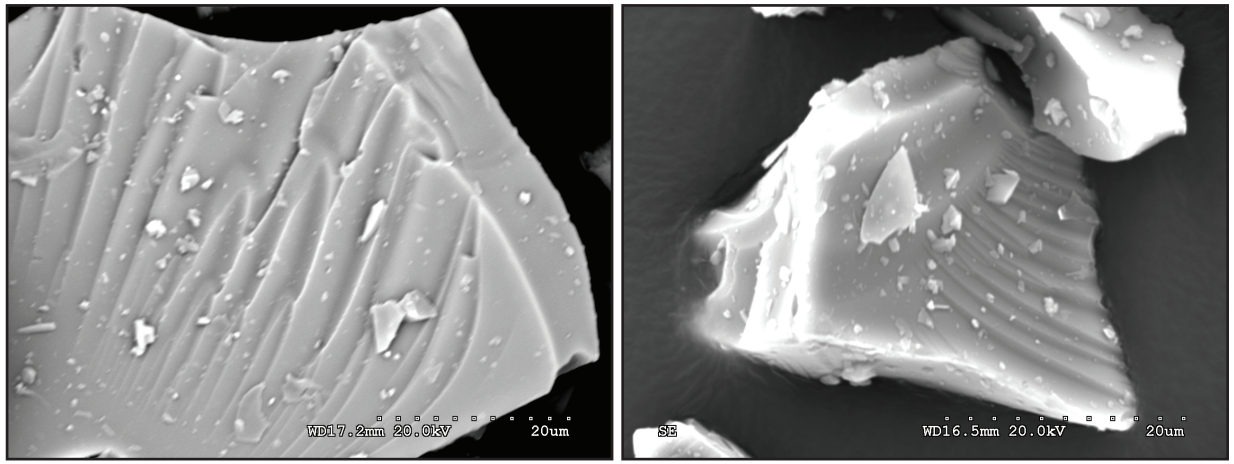

Supplementary Figure S3. Surface fracture patterns (river-lines), resulting from brittle fragmentation under mixed-mode stresses (Hull, 1999).

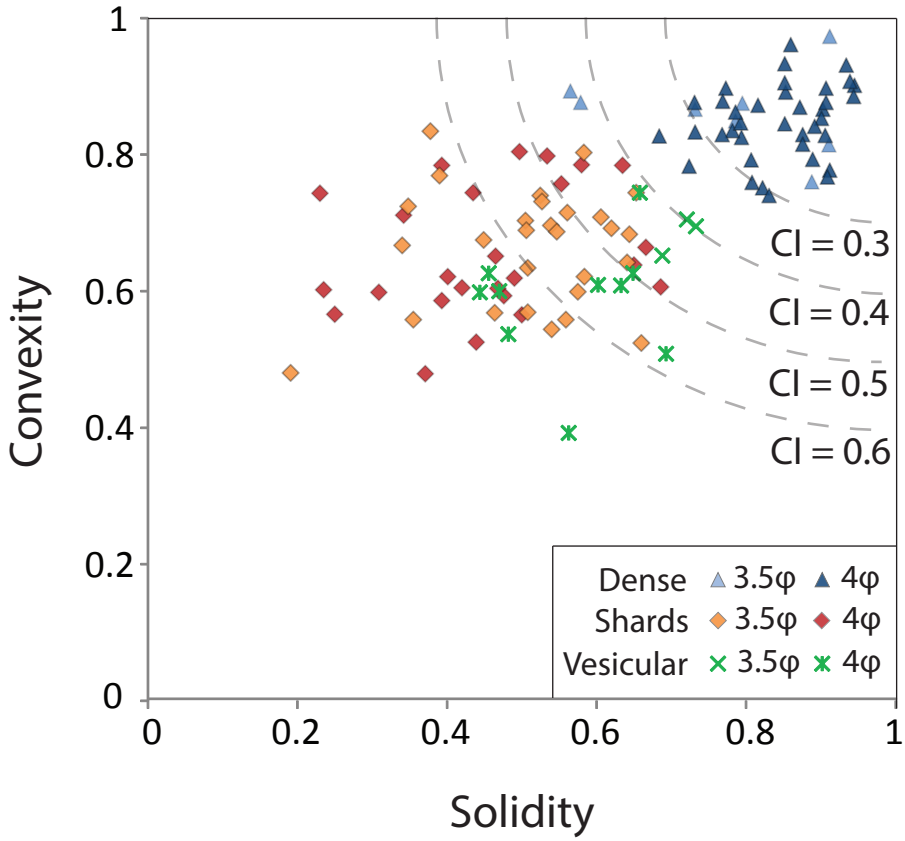

Supplementary information, Figure S4. Origin of the *concavity index*, (*CI*; Eq. 1). Solidity (S) and convexity (C) values are shown for a subsample of ash particles from G6 and G1 (<3.5ϕ and 4ϕ). *CI* is the magnitude of the vector from a perfect circle (S=C=1). The dashed lines show *CI* contours.

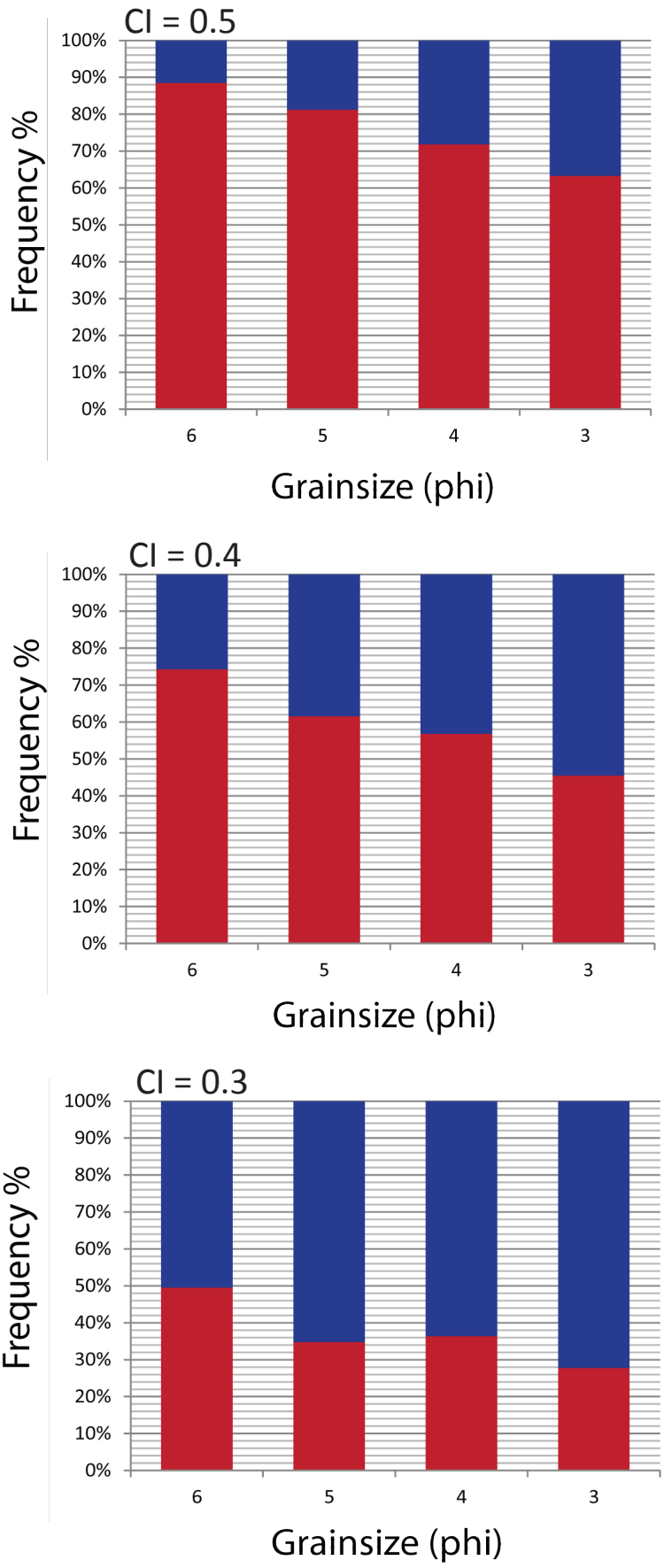

Supplementary information, Figure S5. Sensitivity of automated componentry to *CI* threshold. Manual componentry shown in Figure 3 for comparison. Red and blue bars correspond to dense fragments and bubbly grains (vesicular particles and shards), respectively.

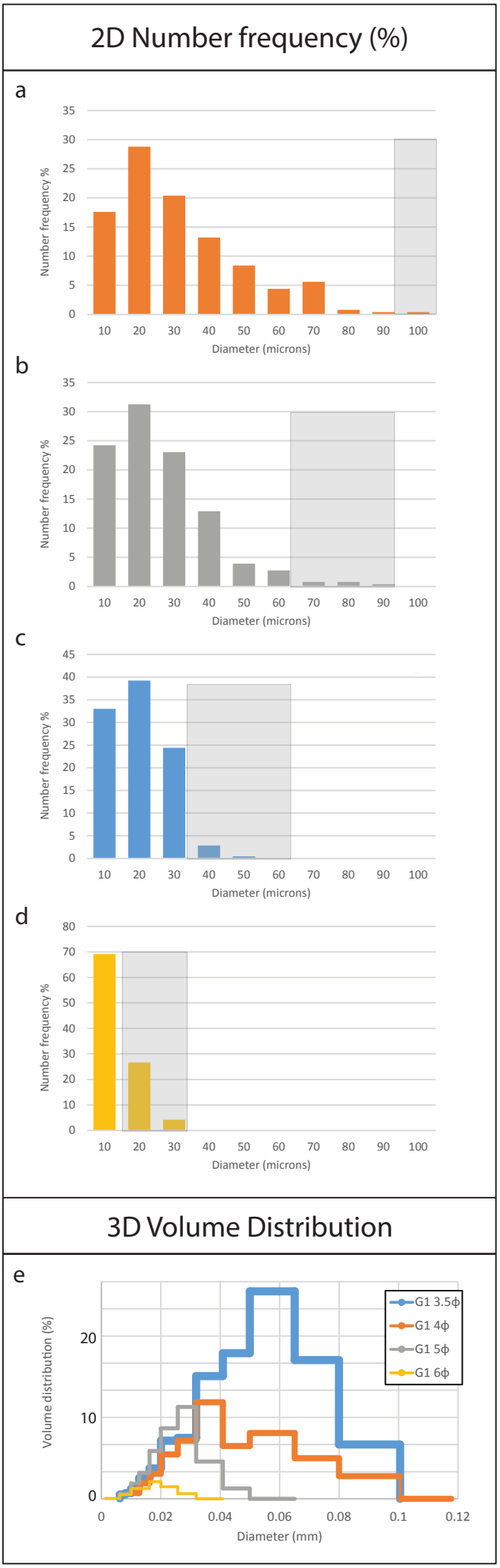

Supplementary information, Figure S6. A-D: Comparison of 2D number frequency of bubble diameters recorded by each ash size fraction (shaded regions indicate size range of particles). The distribution preserved in the coarsest ash fraction does not appear to be truncated, and therefore provides a representative measure of the lower end of the bubble size distribution. E: 3D bubble volume distributions recorded by each ash size class. Distributions are shown as percentages of the total bubble volume. For smaller size classes (4, 5 and 6 phi), distributions are shown as percentages of the total volume of bubbles smaller than the maximum grain size in each size class. Line colours refer to the same particle size classes as shown in A-D.

Supplementary Information

Table S1: Table S1: EPMA glass analyses of ash grains (1 analysis per particle) from the 3φ size fraction of G1 (analyses 1–15) and G6 (analyses 16–28) Grimsvötn samples (22 May 2011).

Analysis No.	SiO_2	TiO_2	Al_2O_3	FeO	MnO	MgO	CaO	Na_2O	K_2O	P_2O_5	SO_2	Cl	Total
1	51.393	2.879	13.458	13.412	0.147	5.322	9.938	1.749	0.524	0.324	0.082	0.004	99.233
2	50.058	2.875	12.727	13.657	0.246	5.717	9.903	2.854	0.481	0.342	0.101	0.030	98.992
3	49.907	3.010	13.113	13.722	0.255	4.895	9.506	2.876	0.538	0.358	0.094	0.024	98.298
4	51.277	2.621	13.610	13.167	0.243	5.606	10.218	3.247	0.587	0.309	0.174	0.012	101.071
5	50.768	3.025	12.841	14.127	0.228	4.938	9.432	2.773	0.546	0.328	0.112	0.006	99.122
6	50.311	2.670	13.422	12.793	0.239	5.550	10.081	2.772	0.497	0.353	0.101	0.009	98.799
7	50.631	2.708	13.403	13.010	0.202	5.327	9.958	2.816	0.473	0.313	0.082	0.019	98.942
8	50.557	3.094	12.996	14.315	0.217	4.979	9.507	2.883	0.523	0.306	0.120	0.029	99.528
9	50.314	2.660	13.479	13.041	0.166	5.685	9.796	2.625	0.430	0.306	0.114	0.006	98.622
10	51.001	2.638	13.519	12.593	0.287	5.529	10.010	2.499	0.463	0.282	0.066	0.020	98.908
11	50.296	2.593	13.267	13.064	0.298	5.662	10.061	2.882	0.452	0.327	0.149	0.017	99.068
12	49.606	2.978	12.816	14.403	0.238	5.165	9.885	2.980	0.508	0.355	0.129	0.009	99.073
13	50.156	2.701	13.414	12.833	0.164	5.569	10.017	2.668	0.430	0.297	0.100	0.021	98.369
14	49.730	2.859	13.158	13.759	0.138	5.377	9.966	2.449	0.544	0.328	0.132	0.026	98.466
15	50.315	3.086	12.972	14.474	0.214	5.088	9.587	2.685	0.528	0.307	0.080	0.031	99.366
16	49.989	3.043	12.992	13.419	0.199	5.262	9.975	3.144	0.471	0.294	0.108	0.019	98.916
17	50.792	3.164	12.640	14.507	0.233	4.980	9.573	2.839	0.512	0.358	0.147	0.014	99.758
18	49.696	2.993	13.044	14.023	0.269	5.126	9.663	2.979	0.486	0.358	0.169	0.034	98.840
19	50.067	2.812	13.168	13.440	0.199	5.348	9.824	2.631	0.428	0.397	0.107	0.022	98.442
20	50.027	2.827	13.325	13.122	0.223	5.436	9.994	2.670	0.420	0.306	0.144	0.000	98.496

21	49.594	3.070	12.730	14.247	0.241	5.217	9.509	2.902	0.476	0.349	0.139	0.023	98.498
22	50.304	2.859	12.927	13.849	0.324	5.444	9.750	3.103	0.429	0.341	0.161	0.022	99.512
23	50.101	2.745	13.356	13.070	0.267	5.530	9.782	2.715	0.507	0.344	0.096	0.014	98.525
24	49.750	3.295	12.312	14.902	0.310	4.876	9.682	2.933	0.545	0.447	0.045	0.021	99.121
25	51.370	1.958	14.198	11.438	0.188	5.702	10.317	2.884	0.483	0.249	0.047	0.000	98.833
26	49.898	2.835	13.137	13.458	0.218	5.098	9.899	2.885	0.515	0.318	0.089	0.011	98.360
27	52.236	2.028	14.230	11.528	0.146	5.235	9.865	2.723	0.497	0.308	0.069	0.028	98.894
28	49.928	3.058	13.147	13.980	0.166	5.191	9.915	2.904	0.505	0.391	0.114	0.004	99.302
Mean	50.439	2.642	14.322	12.646	0.212	4.974	10.106	2.843	0.464	0.311	0.102	0.017	
SD	0.753	0.750	4.321	3.261	0.066	1.327	1.034	0.366	0.115	0.088	0.043	0.009	
SE	0.137	0.137	0.789	0.595	0.012	0.242	0.189	0.067	0.021	0.016	0.008	0.002	

Table S2: Number of particles analysed per size fraction for automated componentry. Automated BSE grid images, each containing 1159–3769 particles in 20–40 images, were acquired for each sample size fraction, with the acquisition magnification set for a minimum resolution of 500 pixels/particle; the average resolution for all size fractions is 2211 pixels/particle. High resolution (average ~20,000 pixels/particle; ≤ 81 images) grids of samples G6 (3.5φ and 4φ) and G1 (4φ) allowed us to test the sensitivity of the shape parameters to image resolution. All images were obtained using a Hitachi S-3500N SEM at the University of Bristol, UK.

Sample	**3.5φ**	**4φ**	**5φ**	**6φ**
G1	1157	2674	2687	2423
G3	2439	1489	1578	1489
G4	1828	1398	1086	1220
G6	1159	1267	2570	2873
G7	2628	1219	1902	2249
G8	2691	1424	1425	1625

Table S3: Grain size distribution data tables. This file contains the raw data and corresponding references for the grain size distributions shown in Figure 1.

Additional references for supplementary information:

Andronico, D., Scollo, S., Lo Castro, M. D., Cristaldi, A., Lodato, L., & Taddeucci, J., 2014b, Eruption dynamics and tephra dispersal from the 24 November 2006 paroxysm at

South-East Crater, Mt Etna, Italy: Journal of Volcanology and Geothermal Research, 274, 78-91.

Andronico, D., Scollo, S., Cristaldi, A., & Castro, M. D. L., 2014a, Representivity of incompletely sampled fall deposits in estimating eruption source parameters: a test using the 12–13 January 2011 lava fountain deposit from Mt. Etna volcano, Italy: Bulletin of Volcanology, 76(10), 1-14.

Büttner, R., Dellino, P., Raue, H., Sonder, I., & Zimanowski, B., 2006, Stress-induced brittle fragmentation of magmatic melts: Theory and experiments: Journal of Geophysical Research: Solid Earth (1978–2012), 111(B8).

Houghton, B.F., & Hackett, W.R., 1984, Strombolian and phreatomagmatic deposits of Ohakune Craters, Ruapehu, New Zealand: a complex interaction between external water and rising basaltic magma: Journal of volcanology and geothermal research, 21(3), 207-231.

Houghton, B.F., & Nairn, I.A., 1991, The 1976–1982 Strombolian and phreatomagmatic eruptions of White Island, New Zealand: eruptive and depositional mechanisms at a 'wet'volcano: Bulletin of volcanology, 54(1), 25-49.

Jude-Eton, T. C., Thordarson, T., Gudmundsson, M. T., & Oddsson, B., 2012, Dynamics, stratigraphy and proximal dispersal of supraglacial tephra during the ice-confined 2004 eruption at Grímsvötn Volcano, Iceland: Bulletin of volcanology, 74(5), 1057-1082.

Mannen, K., 2006, Total grain size distribution of a mafic subplinian tephra, TB-2, from the 1986 Izu-Oshima eruption, Japan: An estimation based on a theoretical model of tephra dispersal: Journal of volcanology and geothermal research, 155(1), 1-17.

Mastin, L.G., Spieler, O., & Downey, W.S., 2009, An experimental study of hydromagmatic fragmentation through energetic, non-explosive magma–water mixing: Journal of Volcanology and Geothermal Research, 180(2), 161-170.

Németh, K., & Cronin, S.J., 2011, Drivers of explosivity and elevated hazard in basaltic fissure eruptions: the 1913 eruption of Ambrym Volcano, Vanuatu (SW-Pacific): Journal of volcanology and geothermal research, 201(1), 194-209.

Olsson, J., Stipp, S.L.S., Dalby, K.N., & Gislason, S.R., 2013, Rapid release of metal salts and nutrients from the 2011 Grímsvötn, Iceland volcanic ash: Geochimica et Cosmochimica Acta, 123, 134-149.

Parfitt, E.A., 1998, A study of clast size distribution, ash deposition and fragmentation in a Hawaiian-style volcanic eruption: Journal of Volcanology and Geothermal Research, 84(3), 197-208.

Porritt, L. A., Russell, J.K., & Quane, S.L., 2012, Pele's tears and spheres: Examples from Kilauea Iki: Earth and Planetary Science Letters, 333, 171-180.

Rose, W.I., Bonis, S., Stoiber, R.E., Keller, M., & Bickford, T., 1973, Studies of volcanic ash from two recent Central American eruptions: Bulletin Volcanologique, 37(3), 338-364

Self, S., Sparks, R.S.J., Booth, B., & Walker, G.P.L., 1974, The 1973 Heimaey strombolian scoria deposit, Iceland: Geological Magazine, 111(06), 539-548.

Stovall, W.K., Houghton, B.F., Gonnermann, H., Fagents, S.A., & Swanson, D.A., 2011, Eruption dynamics of Hawaiian-style fountains: the case study of episode 1 of the Kīlauea Iki 1959 eruption: Bulletin of volcanology, 73(5), 511-529.

Zimanowski, B., Büttner, R., Lorenz, V. & Häfele, H.G., 1997, Fragmentation of basaltic

melt in the course of explosive volcanism: Journal of Geophysical Research - Solid Earth, 102(B1), 803-814.